

# 1 Construction of fault geometry by finite-fault inversion of 2 teleseismic data

3 Kousuke Shimizu,<sup>1</sup> Yuji Yagi,<sup>2</sup> Ryo Okuwaki,<sup>2,3,4</sup> and Yukitoshi Fukahata<sup>5</sup>

<sup>1</sup>*Graduate School of Life and Environmental Sciences, University of Tsukuba, Tsukuba, Ibaraki 305-8572, Japan.*

*E-mail: seismo55smz@gmail.com*

<sup>2</sup>*Faculty of Life and Environmental Sciences, University of Tsukuba, Tsukuba, Ibaraki 305-8572, Japan.*

<sup>3</sup>*Mountain Science Center, University of Tsukuba, Tsukuba, Ibaraki 305-8572, Japan.*

<sup>4</sup>*COMET, School of Earth and Environment, University of Leeds, Leeds LS2 9JT, UK.*

<sup>5</sup>*Disaster Prevention Research Institute, Kyoto University, Uji, Kyoto 611-0011, Japan.*

## 4 5 SUMMARY

6 Conventional seismic source inversion estimates the earthquake rupture process on an as-  
7 sumed fault plane that is determined a priori. It has been a difficult challenge to obtain the  
8 fault geometry together with the rupture process by seismic source inversion because of  
9 the nonlinearity of the inversion technique. In this study, we propose an inversion method  
10 to estimate the fault geometry and the rupture process of an earthquake from teleseismic  
11 *P* waveform data, through an elaboration of our previously published finite-fault inver-  
12 sion analysis (Shimizu et al. 2020). That method differs from conventional methods by  
13 representing slip on a fault plane with five basis double-couple components, expressed  
14 by potency density tensors, instead of two double-couple components compatible with  
15 the fault direction. Because the slip direction obtained from the potency density tensors  
16 should be compatible with the fault direction, we can obtain the fault geometry consis-  
17 tent with the rupture process. In practice we rely on an iterative process, first assuming  
18 a flat fault plane and then updating the fault geometry by using the information included

19 in the obtained potency density tensors. In constructing a non-flat model-fault plane, we  
20 assume for simplicity that the fault direction changes only in either the strike or the dip  
21 direction. After checking the validity of the proposed method through synthetic tests, we  
22 applied it to the  $M_W$  7.7 2013 Balochistan, Pakistan, and  $M_W$  7.9 2015 Gorkha, Nepal,  
23 earthquakes, which occurred along geometrically complex fault systems. The modelled  
24 fault for the Balochistan earthquake is a curved strike-slip fault convex to the south-east,  
25 which is consistent with the observed surface ruptures. The modelled fault for the Gorkha  
26 earthquake is a reverse fault with a ramp-flat-ramp structure, which is also consistent with  
27 the fault geometry derived from geodetic and geological data. These results exhibit that  
28 the proposed method works well for constraining fault geometry of an earthquake.

29 **Key words:** Image processing; Waveform inversion; Inverse theory; Earthquake dynam-  
30 ics; Earthquake source observations

## 31 1 INTRODUCTION

32 The geometry of an earthquake fault reflects a stress field arising from regional tectonics. In mountain-  
33 ous areas, for example, fault geometry tends to be non-planar (e.g. [Fielding et al. 2013](#); [Avouac et al.](#)  
34 [2014](#); [Elliott et al. 2016](#)), which is related to the topography and growth process of mountains (e.g. [El-](#)  
35 [liott et al. 2016](#)). It has also been shown that spatial variations in the fault geometry play an important  
36 role in rupture propagation (e.g. [Aki 1979](#); [Wald & Heaton 1994](#); [Okuwaki & Yagi 2018](#); [Okuwaki](#)  
37 [et al. 2020](#)). Thus, fault geometry has important information that adds detail to our understanding of  
38 regional tectonics and rupture behaviour.

39 The seismic waveform typically contains information on both rupture propagation and fault ge-  
40 ometry underground. Multiple point source inversions have been developed to estimate focal mecha-  
41 nisms and source locations of subevents of large rupture events from seismic waveforms (e.g. [Kikuchi](#)  
42 [& Kanamori 1991](#); [Duputel et al. 2012a,b](#); [Duputel & Rivera 2017](#); [Shi et al. 2018](#); [Yue & Lay 2020](#)).  
43 Although this technique allows us to roughly track rupture propagation from the locations of several  
44 point sources, rupture propagation between subevents cannot be well resolved, obscuring the details  
45 of rupture propagation and its relationship to fault geometry.

46 Finite-fault inversion of seismic waveforms has been widely used for resolving rupture propaga-  
47 tion in detail along a model fault plane (e.g. [Olson & Apsel 1982](#); [Hartzell & Heaton 1983](#)). However,  
48 it had been generally difficult to constrain the fault geometry of an earthquake solely by using it be-

49 cause of strong nonlinearity in the inversion analysis (Fukahata & Wright 2008; Asano & Iwata 2009).  
50 An inappropriate assumption of fault geometry increases modelling errors, which may greatly distort  
51 solutions (e.g. Ragon et al. 2018; Shimizu et al. 2020).

52 In a recent paper, we refined the method of Yagi & Fukahata (2011), which explicitly introduced  
53 uncertainty of Green's functions into seismic source inversion, to develop a novel method of finite-fault  
54 inversion that extracts information on fault geometry as well as rupture propagation from teleseismic  
55  $P$  waveforms (Shimizu et al. 2020). The key to the method is that it adopts five basis double-couple  
56 components (Kikuchi & Kanamori 1991), which are not restricted to the two slip components com-  
57 patible with the fault direction, to represent fault slip. Of course, the true fault geometry should be  
58 compatible with the actual slip direction, but because the teleseismic  $P$ -wave Green's function is in-  
59 sensitive to slight changes in the absolute source location, the new inversion method enables us to infer  
60 the spatiotemporal distribution of potency density tensors (e.g. Ampuero & Dahlen 2005) along the  
61 assumed model fault plane. Potency density tensors, which are obtained by dividing a moment density  
62 tensor by rigidity, contain information on the direction of fault displacement.

63 However, the locations of potency density tensors estimated on an assumed model fault plane can  
64 deviate from their true location, which means that the spatial distribution of the strike and dip angles  
65 of potency density tensors cannot directly yield the fault geometry. Moreover, the estimated potency  
66 density cannot be directly interpreted as slip because the assumed model plane is not always identical  
67 to the real fault plane. Rupture propagation velocity and its relation to fault geometry are also difficult  
68 to properly understand. Thus, source models obtained by the inversion method of Shimizu et al. (2020)  
69 may not be interpreted in the same way as those obtained by conventional inversion methods, in which  
70 a shear slip direction is fixed on the assumed model fault plane.

71 Here, we propose an iterative inversion method to construct fault geometry from teleseismic  $P$   
72 waveforms that uses the method of Shimizu et al. (2020) to solve the spatial distribution of strike and  
73 dip angles on the assumed fault. Iterative solutions allow us to update the fault geometry step by step,  
74 yielding a fault geometry that is consistent with the spatial distribution of strike and dip angles. With  
75 an improved source model, we can better estimate the relationship between rupture propagation and  
76 fault geometry. This paper reports our evaluation of the proposed method through synthetic tests and  
77 our successful application of it to waveforms of the  $M_W$  7.7 2013 Balochistan, Pakistan and the  $M_W$   
78 7.9 2015 Gorkha, Nepal, earthquakes, which occurred on well-characterised, geometrically complex  
79 fault systems.

## 80 2 METHOD

81 We used the inversion method of [Shimizu et al. \(2020\)](#) to construct fault geometries consistent with  
 82 the spatial distribution of the strike or dip of the obtained potency density tensors. Since the potency  
 83 density tensors obtained by the inversion method of [Shimizu et al. \(2020\)](#) depend to some degree on  
 84 the assumed model fault geometry, we used the inversion analysis iteratively to construct the fault  
 85 geometry, at each step solving the spatial distribution of potency density tensors on the assumed fault  
 86 plane. In this study, we assumed for simplicity that the fault geometry changes only either along strike  
 87 or along dip. This assumption leads to two types of model fault: a vertical fault with variable strike  
 88 and uniform dip direction, and a nonvertical fault with variable dip and uniform strike. The proposed  
 89 method follows four steps.

90 Step 1: Set an initial model fault plane

91 The initial model fault is a single flat plane, which is placed to roughly cover the possible source region  
 92 of an earthquake (Step 1 in Fig. 1). The model fault is discretized into a number of flat subfaults evenly  
 93 spaced along the strike and dip directions, with each subfault identical in strike and dip to the model  
 94 fault plane. The initial rupture point coincides with the earthquake hypocentre obtained from other  
 95 studies.

96 Step 2: Perform a potency density tensor inversion

97 The finite-fault inversion of [Shimizu et al. \(2020\)](#) is performed to obtain the spatial distribution of po-  
 98 tency density tensors on the initial model fault plane. Displacement of a seismic waveform  $u_j$  observed  
 99 at a far-field station  $j$  is represented by a linear combination of potency rate density functions of five  
 100 basis double-couple components ([Kikuchi & Kanamori 1991](#)) on the assumed model fault plane  $S$ :

$$u_j = \sum_{q=1}^5 \int_S G_{qj}(t, \xi) * \dot{D}_q(t, \xi) d\xi + e_{bj}(t), \quad (1)$$

101 where  $G_{qj}$  is the Green's function of the  $q$ th basis double-couple component,  $\dot{D}_q$  is the potency rate  
 102 density function of the  $q$ th double-couple component,  $e_{bj}$  is background and instrumental noise,  $\xi$  rep-  
 103 represents a location on the model fault plane  $S$ , and  $*$  is the convolution operator in the time domain. By  
 104 introducing the modelling error of the Green's function into the inversion analysis ([Yagi & Fukahata](#)  
 105 [2011](#)), the potency rate density function is stably obtained from observed waveforms ([Shimizu et al.](#)  
 106 [2020](#)). The spatial distribution of the potency density tensors is obtained by integrating the potency  
 107 rate density functions with respect to time.

108 Step 3: Estimate strike/dip along the model fault

109 In this study, we considered that a fault plane has curvature only along the strike, in which case the  
 110 fault has a uniform dip, or has curvature only along the dip direction, in which case the fault has a

111 uniform strike. We calculate the average of the estimated potency density tensors along the direction  
 112 in which the fault is not curved. Thus, for example, along the strike direction of the model fault plane,  
 113 we obtain focal mechanisms averaged in the dip direction (Step 2 in Fig. 1). To construct a model  
 114 fault plane, we must select one of the two nodal planes determined by the averaged focal mechanism,  
 115 which we do for each subfault by calculating the inner product between the normal vectors of the two  
 116 nodal planes and the normal vector of a reference plane defined by the analyst. The nodal plane with  
 117 the larger inner product (in the absolute) value is selected as the realistic fault plane (Step 3 in Fig. 1).

118 Step 4: Update the model fault geometry or finish the iteration

119 Taking the nodal plane selected in step 3 as the direction of the fault plane, we update the fault geom-  
 120 etry by assigning the direction of that nodal plane to the centre of each subfault. We smoothly connect  
 121 the central points of the subfaults by a spline interpolation with a quadratic function  $f_i$ :

$$\begin{aligned} y &= f_i(x), \\ f_i(x) &= a_i(x - x_i)^2 + b_i(x - x_i) + c_i \quad (x_i \leq x \leq x_{i+1}), \\ i &= 1, 2, \dots, N - 1, \end{aligned} \quad (2)$$

122 where  $x$  is the distance from the hypocentre along the strike/dip direction of the initial flat model plane,  
 123  $y$  is the displacement of the model fault plane perpendicular to the initial flat model plane, and  $N$  is  
 124 the number of subfaults along the strike/dip. The  $x_i$  term, which corresponds to a knot of the quadratic  
 125 function  $f_i$ , is the  $x$  coordinate of the central point of the  $i$ th subfault along the strike/dip.

126 Here, the unknown parameters are  $a_i$ ,  $b_i$ , and  $c_i$ ; the total number of them is  $3(N - 1)$ . The displacement  
 127  $y$  and its derivative are continuous at the nodes from  $i = 2$  to  $N - 1$ :

$$\begin{aligned} f_{i-1}(x_i) &= f_i(x_i), \\ f'_{i-1}(x_i) &= f'_i(x_i), \\ i &= 2, 3, \dots, N - 1. \end{aligned} \quad (3)$$

128 The number of these conditions is  $2(N - 2)$ . In addition, the gradient of the fault plane at each knot is  
 129 given by the direction of the nodal plane selected in step 3:

$$\begin{aligned} y'(x_i) &= d_i, \\ i &= 1, 2, \dots, N, \end{aligned} \quad (4)$$

130 where  $d_i$  represents the gradient of the fault plane at the  $i$ th subfault along the strike/dip. The number  
 131 of this condition is  $N$ . Therefore, by fixing the location of the hypocentre (i.e.  $f_i(x) = 0$ ), we can  
 132 uniquely determine the values of  $a_i$ ,  $b_i$ , and  $c_i$  and obtain the updated geometry of the model fault  
 133 plane (Step 4 in Fig. 1).

134 After updating the fault geometry, the model fault plane is discretized into subfaults again. Here, the  
135 grid interval is taken to be the same as the original one and the distance of the strike/dip direction, to  
136 which the fault is bending, is measured not along the original fault strike/dip (the  $x$  axis) but along  
137 the fault plane. The model fault plane obtained in step 4 is used to update the fault geometry, and the  
138 process returns to step 2 (Fig. 1).

139 The iterations end when the strike/dip direction obtained by step 3 is sufficiently close to that of the  
140 model fault plane used in the inversion analysis. The closeness of the two strikes/dips is based on  
141 the inner product between the unit vectors representing the two strikes/dips. When the inner product  
142 averaged over the subfaults along the strike/dip is acceptably close to 1, the model fault plane is  
143 adopted as the fault plane geometry.

144 To sum up, the nonlinear inversion method starts from step 1 and then proceeds from step 2 to 4  
145 iteratively. We assign (step 1) or update (step 4) the fault geometry, with which we solve the potency  
146 density tensor distribution (step 2), and then extract the information from that solution (step 3) to  
147 update the fault geometry (step 4).

### 148 **3 SYNTHETIC TESTS**

149 We performed synthetic tests of the proposed method for a strike-slip fault (case 1) and a dip-slip fault  
150 (case 2). For both cases, we prepared input source models, described below, and calculated synthetic  
151 waveforms by using theoretical Green's functions. In both cases, the slip-rate function at each subfault  
152 was represented as a combination of linear B-spline functions with a time interval of 0.8 s. Theoretical  
153 Green's functions were calculated following the method of [Kikuchi & Kanamori \(1991\)](#) at 0.1 s inter-  
154 vals, where the attenuation time constant  $t^*$  for the  $P$  wave was taken to be 1.0 s. The 1-D near-source  
155 velocity structures for the cases 1 and 2 are listed in Tables S1 and S2 in the Supporting Information,  
156 respectively. In the calculation of synthetic waveforms, we added errors of Green's function and back-  
157 ground noise to synthetic waveforms. As an error of Green's function, we added random Gaussian  
158 noise with zero mean and a standard deviation of 5% of the maximum amplitude of each calculated  
159 Green's function. We then added random Gaussian noise with zero mean and a standard deviation of 1  
160  $\mu\text{m}$  as the background noise. In the inversion process, we resampled the calculated synthetic waveform  
161 data at 0.8 s intervals without applying any filter to either the calculated waveforms or the theoretical  
162 Green's functions.

### 163 3.1 Case 1: Vertical strike-slip fault bending along strike

164 We applied the proposed method for a vertical fault with variable strike and uniform dip direction. The  
 165 fault is composed of two vertical flat fault planes, each one 75 km long and 20 km wide, with strikes  
 166 of  $160^\circ$  and  $200^\circ$ , respectively (Fig. 2a). The slip distribution of the input source model with two slip  
 167 patches is shown in Fig. 2b. The slip direction is pure right lateral. The input slip-rate function at each  
 168 subfault had a total duration of 6 s. The hypocentre location was  $26.900^\circ\text{N}$ ,  $65.400^\circ\text{E}$  at a depth of 7.5  
 169 km. Rupture of each subfault was triggered by the expanding circular rupture front propagating from  
 170 the hypocentre at 3 km/s. Synthetic waveforms were calculated for the selected stations shown in Fig.  
 171 2c.

172 In the inversion analysis, the initial model fault was a vertical plane 150 km long and 20 km wide  
 173 with a strike of  $180^\circ$  (Fig. 3a). The potency rate density functions on this plane were expanded by  
 174 bilinear B-spline functions with a spatial interval of 5 km and by linear B-spline functions with a  
 175 temporal interval of 0.8 s and a total duration of 6 s. The hypocentre was the same one used as the  
 176 input. The maximum rupture front velocity was assumed to be 3 km/s. We adopted a plane with a strike  
 177 of  $354^\circ$  and a dip of  $89^\circ$ , derived from the total potency tensor obtained by a preliminary analysis, as  
 178 the reference plane used for selecting realistic nodal planes.

179 The obtained fault model after two iterations reproduced the straight parts and bend in the input  
 180 fault very well (Fig. 3a). The slip distribution with two slip patches (Fig. 3c) was also consistent with  
 181 the input source model, including the slip direction (Fig. 2b). Testing the model's sensitivity to the  
 182 strike of the initial model plane by changing it to  $170^\circ$  and  $190^\circ$ , we obtained nearly the same results  
 183 (Figs 3 b and c). However, large deviations of the initial fault plane from the true one and the modelling  
 184 error of the Green's function, which increases with distance from the hypocentre, may cause unstable  
 185 estimates of fault geometry, as seen at the southern end of the model fault with  $170^\circ$  strike. These  
 186 results confirm that the proposed method works well for faults with bending along strike when the  
 187 initial model fault plane is reasonably accurate.

### 188 3.2 Case 2: Reverse faulting along a bending fault

189 We applied the proposed method for a nonvertical fault with variable dip and uniform strike. The fault  
 190 is composed of three adjacent planes with different dips (Fig. 4a). The three planes had a  $285^\circ$  strike  
 191 and together extended 65 km; from top to bottom their dips were  $20^\circ$ ,  $0^\circ$  and  $20^\circ$ , and their widths  
 192 were 20 km, 25 km, and 20 km, respectively. The slip distribution of the input source model is shown  
 193 in Fig. 4b. The input slip-rate function at each subfault had a total duration of 10 s. The hypocentre  
 194 location was  $28.231^\circ\text{N}$ ,  $84.731^\circ\text{E}$  at a depth of 15 km. Rupture in each subfault was triggered by

195 the expanding circular rupture front propagating from the hypocentre at 3 km/s. Synthetic waveforms  
196 were calculated for the selected stations shown in Fig. 4c.

197 In the inversion analysis, the initial model fault was a horizontal plane 65 km long and 75 km wide,  
198 and 15 km deep with a strike of  $285^\circ$  and a dip of  $0^\circ$  (Fig. 5b). The potency rate density functions on  
199 this plane were expanded by bilinear B-spline functions with a spatial interval of 5 km and by linear  
200 B-spline functions with a temporal interval of 0.8 s and a total duration of 10 s. The hypocentre was  
201 the same one used as the input. The maximum rupture front velocity was assumed to be 3.0 km/s. We  
202 adopted a plane with a strike of  $273^\circ$  and a dip of  $11^\circ$ , derived from the total potency tensor obtained  
203 by a preliminary analysis, as the reference plane used for selecting realistic nodal planes.

204 The obtained fault model after two iterations, shown in Fig. 5a as a 3-D view and in Fig. 5b  
205 as a cross sectional view, features a dip that ranges from  $4^\circ$  around the hypocentre to  $18^\circ$  and  $19^\circ$   
206 near the up-dip and down-dip edges, respectively. The obtained fault model reproduced the input fault  
207 geometry and its slip distribution well (Fig. 5d), although its geometry was slightly smoother. Testing  
208 the model's sensitivity to the dip of the initial model plane by changing it to  $10^\circ$  and  $20^\circ$ , we obtained  
209 nearly the same results (Figs 5 c and d). These results confirm that the proposed method works well  
210 for faults with bending along dip.

## 211 4 APPLICATION TO REAL WAVEFORMS

212 In order to further examine the validity of the proposed method, we applied it to the  $M_W$  7.7 2013  
213 Balochistan, Pakistan, and the  $M_W$  7.9 2015 Gorkha, Nepal, earthquakes. Fault geometries of the  
214 both earthquakes have been well constrained by previous studies showing that they occurred on non-  
215 planar faults. Thus, these earthquakes provide us opportunities to test whether the proposed method  
216 can reconstruct curved fault geometries.

### 217 4.1 The 2013 Balochistan earthquake

218 The Balochistan earthquake was a strike-slip event as indicated by Global Centroid Moment Tensor  
219 (GCMT; [Dziewonski et al. 1981](#); [Ekström et al. 2012](#), <https://www.globalcmt.org/CMTsearch.html>;  
220 last accessed 17 January 2020) solution and the  $W$ -phase moment tensor solution determined by the  
221 U.S. Geological Survey, National Earthquake Information Center (USGS NEIC; <https://earthquake.usgs.gov/earthquakes/>  
222 last accessed 17 January 2020). Satellite images acquired after the earthquake ([Avouac et al. 2014](#); [Jo-  
223 livet et al. 2014](#); [Zinke et al. 2014](#)) show surface ruptures that describe a curve convex to the south-east.  
224 The teleseismic  $P$ -waveform inversion analysis of [Shimizu et al. \(2020\)](#) yielded a source model sug-



gesting strike-slip faulting in which the strike rotates from  $205^\circ$  at the north end to  $240^\circ$  at the south end.

Our inversion analysis used the observed vertical components of teleseismic  $P$  waveforms at 36 stations shown in Fig. 2c, the same data used by Shimizu et al. (2020). We adopted the USGS epicentre of  $26.900^\circ\text{N}$ ,  $65.400^\circ\text{E}$  and the hypocentral depth of 7.5 km used by Shimizu et al. (2020). Theoretical Green's functions were calculated the same way as the synthetic tests in Section 3, using the 1-D near-source velocity structure (Supporting Information Table. S1) used in Avouac et al. (2014). The initial fault plane was 200 km long and 20 km wide, with a strike of  $230^\circ$  and a dip of  $90^\circ$ , that roughly followed the trace of the surface rupture observed by Zinke et al. (2014) (Fig. 6a). The potency rate density functions on this plane were expanded by bilinear B-spline functions with a spatial interval of 5 km and by linear B-spline functions with a temporal interval of 0.8 s and a total duration of 31 s. We also assumed the maximum rupture-front velocity to be 4 km/s and the potency rate density to be zero after 60 s from the rupture initiation, following the finite-fault inversion analysis of Shimizu et al. (2020). We adopted a plane with a strike of  $226^\circ$  and a dip of  $69^\circ$ , derived from the total potency tensor obtained by a preliminary analysis, as the reference plane used for selecting realistic nodal planes.

The inversion results after the third iteration, shown in Fig. 6, had an excellent fit between the observed and synthetic waveforms at all stations (Supporting Information Fig. S1). The estimated fault trace is 205 km long and curved, with a strike that changes from  $218^\circ$  at the northern edge around 50 km north-east of the epicentre, to  $213^\circ$  around the epicentre, to  $241^\circ$  at the southern edge around 140 km south-west of the epicentre (Fig. 6a). Its geometry is consistent with the surface ruptures observed after the earthquake (Zinke et al. 2014), shown by the grey line in Fig. 6a, though the estimated fault geometry is slightly smoother than the observed surface rupture trace. Focal mechanisms along the fault trace (Fig. 6a), obtained by integrating the potency density tensors (Fig. 6b) along the dip direction, clearly show that strike-slip faulting is dominant. Integrating the potency density tensors (Fig. 6b) over the model fault plane yields the total potency tensor of this earthquake (Fig. 6a), which indicates strike-slip faulting with a strike of  $226^\circ$  and a dip of  $69^\circ$ . The total seismic moment release is  $6.16 \times 10^{20}$  Nm ( $M_W$  7.8), which is comparable to the estimate of  $7.53 \times 10^{20}$  Nm ( $M_W$  7.8) by Shimizu et al. (2020) and the GCMT solution of  $5.59 \times 10^{20}$  Nm ( $M_W$  7.8). The estimated source-time function, with a prominent peak at around 12 s and three minor peaks at around 28, 43, and 58 s (Fig. 6a), is comparable to the result of Shimizu et al. (2020).

Although focal mechanisms have two nodal planes, we could select the realistic fault plane from the focal mechanisms obtained in this inversion analysis by using the reference plane (Figs 6 a and b). Decomposing the potency density tensors at the Earth's surface into the strike-slip component (positive for left-lateral fault slip) and the dip-slip component (positive for reverse fault slip), as shown in Fig.

259 6c, demonstrates that left-lateral strike-slip is predominant, reaching a maximum of 16.3 m near the  
260 epicentre and gradual decrease toward both ends of the fault. The dip-slip component has a maximum  
261 value of 3.0 m at a point 25 km north-east of the epicentre and decreases to  $-1.3$  m at a point 100 km  
262 south-west of the epicentre with small fluctuation (Fig. 6c).

263 Dip angles on the fault plane range from  $57^\circ$  to  $89^\circ$  (Fig. 6d). Dip is recognizably dependent  
264 on depth, being steeper in the shallower part of the fault plane consistent with the idea of a listric  
265 fault, especially around the epicentre and 100 km south-west of the epicentre (Fig. 6d). Around the  
266 epicentre, the dip gradually increases from  $68^\circ$  at 17.5 km depth to  $72^\circ$  at 2.5 km depth (Fig. 6d).  
267 Around 100 km south-west of the epicentre, the depth dependence of the dip angle is clearer than that  
268 around the epicentre; the dip angle increases from  $60^\circ$  at 17.5 km depth to  $71^\circ$  at 2.5 km depth (Fig.  
269 6d).

## 270 4.2 The 2015 Gorkha earthquake

271 Both the GCMT solution (Dziewonski et al. 1981; Ekström et al. 2012) and the  $W$ -phase moment ten-  
272 sor solution determined by the USGS NEIC (<https://earthquake.usgs.gov/earthquakes/eventpage/us20002926>,  
273 last accessed 17 January 2020) indicate that the Gorkha earthquake was a thrust event with a fault sur-  
274 face dipping at  $7^\circ$ . A teleseismic  $P$ -waveform inversion analysis (Yagi & Okuwaki 2015) produced a  
275 finite-fault source model in which the main rupture area is distributed around 50 km east of the epicen-  
276 tre. The Gorkha earthquake has been reported to have occurred along the Main Himalayan Thrust (e.g.  
277 Elliott et al. 2016; Hubbard et al. 2016; Duputel et al. 2016). An analysis of Interferometric Synthetic  
278 Aperture Radar (InSAR) and Global Navigation Satellite System (GNSS) data (Elliott et al. 2016)  
279 showed that the earthquake occurred on a north-dipping fault with a ramp-flat-ramp structure, dipping  
280 at  $30^\circ$  from the surface to 5 km depth,  $7^\circ$  in a relatively flat section 75 km wide, and  $20^\circ$  in the deepest  
281 section 30 km wide. Hubbard et al. (2016) proposed a similar geometric model of the Main Himalayan  
282 Thrust, covering the source area of the Gorkha earthquake, on the basis of geological data in which  
283 the central portion had a  $7^\circ$  dip and the adjoining portions on the up-dip and down-dip sides had a  $26^\circ$   
284 dip. Duputel et al. (2016) also proposed a ramp-flat-ramp fault geometry for the Gorkha earthquake  
285 on the basis of a receiver function analysis.

286 Our inversion analysis used the observed vertical components of teleseismic  $P$  waveforms at the  
287 54 stations shown in Fig. 4c, the same data used by Yagi & Okuwaki (2015). We adopted the USGS  
288 epicentre of  $28.231^\circ\text{N}$ ,  $84.731^\circ\text{E}$  and the hypocentral depth of 15 km used by Yagi & Okuwaki (2015).  
289 Theoretical Green's functions were calculated the same way as the synthetic tests in Section 3, using  
290 the 1-D near-source velocity structure (Supporting Information Table. S2) from the CRUST 1.0 model  
291 (Laske et al. 2013). The initial fault plane was 160 km long and 110 km wide, with a strike of  $285^\circ$  and

292 a dip of  $0^\circ$ , that entirely covered the possible source region estimated by [Yagi & Okuwaki \(2015\)](#) (Fig.  
 293 7a). The potency rate density functions on the model fault plane were expanded by bilinear B-spline  
 294 functions with a spatial interval of 10 km and 5 km along the strike and dip directions, respectively,  
 295 and by linear B-spline functions with a temporal interval of 1.0 s and a total duration of 28 s. We also  
 296 assumed the maximum rupture-front velocity to be 3 km/s and the potency rate density to be zero after  
 297 60 s from the rupture initiation, following [Yagi & Okuwaki \(2015\)](#). We adopted a plane with a strike  
 298 of  $326^\circ$  and a dip of  $8^\circ$ , derived from the total potency tensor obtained by a preliminary analysis, as  
 299 the reference plane used for selecting realistic nodal planes.

300 The inversion results after the third iteration, shown in Fig. 7, had an excellent fit between the  
 301 observed and synthetic waveforms (Supporting Information Fig. S2). The fault plane dips towards the  
 302 north-east and is 105 km wide (Fig. 7b). The spatial distribution of potency density tensors (Fig. 7a)  
 303 shows that the main rupture area ( $>50\%$  of the maximum slip) is distributed around 50 km east of the  
 304 epicentre, where the maximum slip is 5.0 m. The main rupture area is dominated by thrust faulting  
 305 with dips ranging from  $2^\circ$  to  $22^\circ$ . The total potency tensor indicates thrust faulting with a strike of  
 306  $332^\circ$  and a dip of  $9^\circ$  (Fig. 7a). The total seismic moment release is  $9.1 \times 10^{20}$  Nm ( $M_W$  7.9), which  
 307 matches the  $9.1 \times 10^{20}$  Nm ( $M_W$  7.9) estimated by [Yagi & Okuwaki \(2015\)](#). The cross section of the  
 308 estimated fault plane (Fig. 7b), taken perpendicular to the fault strike (the A–B line shown in Fig. 7a),  
 309 shows that the dip changes from  $42^\circ$  at the up-dip edge (45 km south-west of the hypocentre) to a  
 310 minimum of  $6^\circ$  at the hypocentre to  $15^\circ$  at the down-dip edge (55 km north-east of the hypocentre).  
 311 As seen in the 3-D view of the fault model (Fig. 7d), the main rupture area is mostly distributed in the  
 312 part of the fault with lower dip ( $<10^\circ$ ).

## 313 5 DISCUSSION

314 In this study, we proposed a nonlinear inversion method to construct the fault geometry of an earth-  
 315 quake through the development of the finite-fault inversion method of [Shimizu et al. \(2020\)](#). They  
 316 estimated spatial distribution of potency density tensors on an assumed fault plane, from which we  
 317 can extract information on slip direction on the fault plane. Through synthetic tests and application  
 318 to real waveform data, we showed that our proposed method can construct the fault geometry well,  
 319 even if the strike or dip varies along the fault plane. Thus, it is possible to directly compare the ob-  
 320 tained source model with other observed data, as can be done for source models obtained by using  
 321 conventional inversion methods.

322 The clear surface displacements from the Balochistan earthquake documented by [Zinke et al.](#)  
 323 (2014) can be readily compared with our source model (Fig. 6a) and seen to be in good agreement.  
 324 The increased surface displacement around the hypocentre in our model (Fig. 6b) is also consistent

325 with the distribution of surface displacement across the fault trace in satellite images (e.g. [Avouac](#)  
326 [et al. 2014](#); [Zinke et al. 2014](#)). The Arabia plate subducts beneath the Eurasia plate in the southern part  
327 of the Makran accretionary wedge, and active thrust faults exist in the Makran accretionary wedge  
328 ([Haghipour et al. 2012](#)), the site of the Balochistan earthquake hypocentre. The shallowing dip with  
329 increasing depth on the estimated fault plane (Fig. 6d) may suggest that the earthquake ruptured a  
330 thrust fault that has listric geometry.

331 Because the Gorkha earthquake did not produce surface ruptures (e.g. [Avouac et al. 2015](#)), there  
332 are no observational data that can be directly compared with our estimated fault geometry. Our source  
333 model of the Gorkha earthquake has a fault geometry with a ramp-flat-ramp structure (Figs 7 b and d),  
334 which is consistent with the fault geometry modelled by using geophysical and geological data (e.g.  
335 [Elliott et al. 2016](#); [Hubbard et al. 2016](#); [Duputel et al. 2016](#)), although the flat part is narrower in our  
336 model. The estimated slip distribution, with larger slip in the flat part (Figs 7 a and d), is also consistent  
337 with the analysis of InSAR and GNSS data by [Elliott et al. \(2016\)](#). The fault geometry modelled by  
338 [Hubbard et al. \(2016\)](#), using geological knowledge and the slip distribution estimated by [Avouac et al.](#)  
339 [\(2015\)](#), also places the main rupture area in the flat part of the fault. Therefore, our proposed method,  
340 based solely on teleseismic data, yields a source model of the Gorkha earthquake that is comparable to  
341 fault geometry and slip distributions independently estimated from geophysical and structural geology  
342 data.

343 Because our proposed method uses spline interpolation in constructing fault geometry, continuous  
344 and geometrically smooth faults are best suited to this method. Furthermore, a realistic strike or dip  
345 was selected for each subfault on the basis of the similarity of the resolved nodal plane to the single  
346 reference plane. This procedure implicitly assumes that the strike or dip varies by less than  $45^\circ$  be-  
347 cause a rotation of a focal mechanism around its own  $B$  axis greater than  $45^\circ$  places the conjugate  
348 nodal plane closer to the reference plane. This assumption was sound in the cases the Balochistan and  
349 Gorkha earthquakes because the strike and dip of their faults varied by less than  $45^\circ$ . Our proposed  
350 method may be extended to construct a fault geometry with a greater variation of strike or dip than  
351  $45^\circ$  by determining a realistic nodal plane on the basis of the nodal plane of the adjacent subfault and  
352 extending this procedure sequentially in the direction away from the epicentre. On the other hand, it  
353 is difficult to use our proposed method to construct a conjugated fault system or a segmented fault  
354 system, such as the faults of the  $M_W$  7.8 2016 Kaikoura, New Zealand, and the  $M_W$  7.9 2018 Alaska  
355 earthquakes.

356 In each application of our method to both synthetic and real waveforms, it took only a few it-  
357 erations of the finite-fault inversion to reconstruct the fault geometry, which was expected from the  
358 assumption that the fault geometry can be constructed from strike or dip data alone. Although this

359 assumption results in a weak nonlinearity in our method, nonlinearities may also stem from the low  
 360 spatial resolution of teleseismic data and the fact that the uncertainty of the Green's function is taken  
 361 into account in the finite-fault inversion (Shimizu et al. 2020).

## 362 6 CONCLUSIONS

363 We proposed and tested a method of constructing fault geometry that relies on only teleseismic data,  
 364 using a finite-fault inversion iteratively to estimate potency density tensor distributions that can express  
 365 slips in an arbitrary direction. We assumed that an estimated fault plane has bends only along the  
 366 strike or only in the dip direction, which leads to a weak nonlinearity of the method. After testing the  
 367 performance of the method through synthetic tests, we applied this method to the 2013 Balochistan and  
 368 2015 Gorkha earthquakes, which previous studies have shown to have occurred along geometrically  
 369 complex fault systems. For both events, our estimates of the fault geometry were consistent with  
 370 previous studies that analysed different observational data. This method works well for constructing  
 371 the fault geometry of an earthquake that ruptured a geometrically smooth and continuous fault plane.

## 372 ACKNOWLEDGMENTS

373 We thank the editor and the reviewers for their handling and reviewing our manuscript. This work  
 374 was supported by the Japan Society for the Promotion of Science (JSPS) KAKENHI Grant-in-Aid  
 375 for Scientific Research (JP19K04030) and JSPS KAKENHI Grant-in-Aid for Scientific Research  
 376 on Innovative Areas (JP16H06477, JP18H05447). The authors thank Keita Kayano for his valu-  
 377 able comments and suggestions during the early stage of this study. Teleseismic waveforms from the  
 378 networks, GEOSCOPE, Hong Kong Seismographic Network, Global Telemetered Seismograph Net-  
 379 work (USAF/USGS), New China Digital Seismograph Network, Global Seismograph Network (GSN-  
 380 IRIS/IDA), Global Seismograph Network (GSN-IRIS/USGS), the Canadian National Seismograph  
 381 Network, Czech Regional Seismic Network, GEOFON, the MEDNET Project, Pacific21, and the  
 382 United States National Seismic Network, were downloaded from the IRIS-DMC website (<https://ds.iris.edu/ds/nodes/dmc/>)  
 383 All the figures were created with matplotlib (Hunter 2007, Version 3.2.1; <https://doi.org/10.5281/zenodo.3714460>)  
 384 and ObsPy (Krischer et al. 2015; Megies et al. 2011; Beyreuther et al. 2010, Version 1.2.1; <http://doi.org/10.5281/zenodo.3714460>)

## 386 REFERENCES

387 Aki, K., 1979. Characterization of barriers on an earthquake fault, *Journal of Geophysical Research: Solid*  
 388 *Earth*, **84**(B11), 6140–6148.

- 389 Ampuero, J. P. & Dahlen, F. A., 2005. Ambiguity of the moment tensor, *Bulletin of the Seismological Society*  
390 *of America*, **95**(2), 390–400.
- 391 Asano, K. & Iwata, T., 2009. Kinematic Source Inversion using Strong Motion Data Considering Three-  
392 Dimensional Fault Geometry, in *AGU Fall Meeting Abstracts*, vol. 2009, pp. S31A–1688.
- 393 Avouac, J. P., Ayoub, F., Wei, S., Ampuero, J. P., Meng, L., Leprince, S., Jolivet, R., Duputel, Z., & Helmberger,  
394 D., 2014. The 2013, Mw 7.7 Balochistan earthquake, energetic strike-slip reactivation of a thrust fault, *Earth*  
395 *and Planetary Science Letters*, **391**, 128–134.
- 396 Avouac, J.-P., Meng, L., Wei, S., Wang, T., & Ampuero, J.-P., 2015. Lower edge of locked Main Himalayan  
397 Thrust unzipped by the 2015 Gorkha earthquake, *Nature Geoscience*, **8**(9), 708–711.
- 398 Beyreuther, M., Barsch, R., Krischer, L., Megies, T., Behr, Y., & Wassermann, J., 2010. ObsPy: A Python  
399 Toolbox for Seismology, *Seismological Research Letters*, **81**(3), 530–533.
- 400 Duputel, Z. & Rivera, L., 2017. Long-period analysis of the 2016 Kaikoura earthquake, *Physics of the Earth*  
401 *and Planetary Interiors*, **265**, 62–66.
- 402 Duputel, Z., Kanamori, H., Tsai, V. C., Rivera, L., Meng, L., Ampuero, J. P., & Stock, J. M., 2012a. The 2012  
403 Sumatra great earthquake sequence, *Earth and Planetary Science Letters*, **351-352**, 247–257.
- 404 Duputel, Z., Rivera, L., Kanamori, H., & Hayes, G., 2012b. W phase source inversion for moderate to large  
405 earthquakes (1990-2010), *Geophysical Journal International*, **189**(2), 1125–1147.
- 406 Duputel, Z., Vergne, J., Rivera, L., Wittlinger, G., Farra, V., & Hetényi, G., 2016. The 2015 Gorkha earthquake:  
407 A large event illuminating the Main Himalayan Thrust fault, *Geophysical Research Letters*, **43**(6), 2517–  
408 2525.
- 409 Dziewonski, A. M., Chou, T., & Woodhouse, J., 1981. Determination of earthquake source parameters from  
410 waveform data for studies of global and regional seismicity, *Journal of Geophysical Research: Solid Earth*,  
411 **86**(B4), 2825–2852.
- 412 Ekström, G., Nettles, M., & Dziewoński, A. M., 2012. The global CMT project 2004 - 2010: Centroid-  
413 moment tensors for 13,017 earthquakes, *Physics of the Earth and Planetary Interiors*, **200-201**, 1–9.
- 414 Elliott, J. R., Jolivet, R., Gonzalez, P. J., Avouac, J. P., Hollingsworth, J., Searle, M. P., & Stevens, V. L.,  
415 2016. Himalayan megathrust geometry and relation to topography revealed by the Gorkha earthquake, *Nature*  
416 *Geoscience*, **9**(2), 174–180.
- 417 Fielding, E. J., Sladen, A., Li, Z., Avouac, J. P., Bürgmann, R., & Ryder, I., 2013. Kinematic fault slip  
418 evolution source models of the 2008 M7.9 wenchuan earthquake in china from SAR interferometry, GPS  
419 and teleseismic analysis and implications for longmen shan tectonics, *Geophysical Journal International*,  
420 **194**(2), 1138–1166.
- 421 Fukahata, Y. & Wright, T. J., 2008. A non-linear geodetic data inversion using ABIC for slip distribution on a  
422 fault with an unknown dip angle, *Geophysical Journal International*, **173**(2), 353–364.
- 423 Haghypour, N., Burg, J. P., Kober, F., Zeilinger, G., Ivy-Ochs, S., Kubik, P. W., & Faridi, M., 2012. Rate of  
424 crustal shortening and non-Coulomb behaviour of an active accretionary wedge: The folded fluvial terraces  
425 in Makran (SE, Iran), *Earth and Planetary Science Letters*, **355-356**, 187–198.

- 426 Hartzell, S. H. & Heaton, T. H., 1983. Inversion of strong ground motion and teleseismic waveform data for  
427 the fault rupture history of the 1979 Imperial Valley, California, earthquake, *Bulletin of the Seismological*  
428 *Society of America*, **73**(6), 1553–1583.
- 429 Hubbard, J., Almeida, R., Foster, A., Sapkota, S. N., Bürgi, P., & Tapponnier, P., 2016. Structural segmentation  
430 controlled the 2015 MW 7.8 Gorkha earthquake rupture in Nepal, *Geology*, **44**(8), 639–642.
- 431 Hunter, J. D., 2007. Matplotlib: A 2D graphics environment, *Computing in Science & Engineering*, **9**(3),  
432 90–95.
- 433 Jolivet, R., Duputel, Z., Riel, B., Simons, M., Rivera, L., Minson, S. E., Zhang, H., Aivazis, M. A., Ayoub, F.,  
434 Leprince, S., Samsonov, S., Motagh, M., & Fielding, E. J., 2014. The 2013 Mw7.7 Balochistan earthquake:  
435 Seismic potential of an accretionary wedge, *Bulletin of the Seismological Society of America*, **104**(2), 1020–  
436 1030.
- 437 Kikuchi, M. & Kanamori, H., 1991. Inversion of Complex Body Waves-III, *Bulletin of the Seismological*  
438 *Society of America*, **81**(6), 2335–2350.
- 439 Krischer, L., Megies, T., Barsch, R., Beyreuther, M., Lecocq, T., Caudron, C., & Wassermann, J., 2015. ObsPy:  
440 a bridge for seismology into the scientific Python ecosystem, *Computational Science & Discovery*, **8**(1),  
441 14003.
- 442 Laske, G., Masters, G., Ma, Z., & Pasyanos, M., 2013. Update on CRUST1.0—A 1-degree global model of  
443 Earth's crust, *EGU General Assembly 2013*, **15**, 2658.
- 444 Megies, T., Beyreuther, M., Barsch, R., Krischer, L., & Wassermann, J., 2011. ObsPy - What can it do for  
445 data centers and observatories?, *Annals of Geophysics*, **54**(1), 47–58.
- 446 Okuwaki, R. & Yagi, Y., 2018. Role of geometric barriers in irregular-rupture evolution during the 2008  
447 Wenchuan earthquake, *Geophysical Journal International*, **212**(3), 1657–1664.
- 448 Okuwaki, R., Hirano, S., Yagi, Y., & Shimizu, K., 2020. Inchworm-like source evolution through a geo-  
449 metrically complex fault fueled persistent supershear rupture during the 2018 Palu Indonesia earthquake,  
450 *EarthArXiv*.
- 451 Olson, A. H. & Apsel, R. J., 1982. Finite faults and inverse theory with applications to the 1979 Imperial  
452 Valley earthquake, *Bulletin of the Seismological Society of America*, **72**(6), 1969–2001.
- 453 Ragon, T., Sladen, A., & Simons, M., 2018. Accounting for uncertain fault geometry in earthquake source  
454 inversions - I: theory and simplified application, *Geophysical Journal International*, **214**, 1174–1190.
- 455 Shi, Q., Wei, S., & Chen, M., 2018. An MCMC multiple point sources inversion scheme and its application to  
456 the 2016 Kumamoto Mw 6.2 earthquake, *Geophysical Journal International*, **215**(2), 737–752.
- 457 Shimizu, K., Yagi, Y., Okuwaki, R., & Fukahata, Y., 2020. Development of an inversion method to extract  
458 information on fault geometry from teleseismic data, *Geophysical Journal International*, **220**(2), 1055–1065.
- 459 Wald, D. J. & Heaton, T. H., 1994. Spatial and temporal distribution of slip for the 1992 Landers, California,  
460 earthquake, *Bulletin of the Seismological Society of America*, **84**(3), 668–691.
- 461 Yagi, Y. & Fukahata, Y., 2011. Introduction of uncertainty of Green's function into waveform inversion for  
462 seismic source processes, *Geophysical Journal International*, **186**(2), 711–720.

- 463 Yagi, Y. & Okuwaki, R., 2015. Integrated seismic source model of the 2015 Gorkha, Nepal, earthquake,  
464 *Geophysical Research Letters*, **42**(15), 6229–6235.
- 465 Yue, H. & Lay, T., 2020. Resolving Complicated Faulting Process Using Multi-Point-Source Representation:  
466 Iterative Inversion Algorithm Improvement and Application to Recent Complex Earthquakes, *Journal of*  
467 *Geophysical Research: Solid Earth*, **125**(2), 1–24.
- 468 Zinke, R., Hollingsworth, J., & Dolan, J. F., 2014. Surface slip and off-fault deformation patterns in the  
469 2013 Mw7.7 Balochistan, Pakistan earthquake: Implications for controls on the distribution of near-surface  
470 coseismic slip, *Geochemistry, Geophysics, Geosystems*, **15**(12), 5034–5050.

471 **SUPPORTING INFORMATION**

472 **Figure S1.** Fitting between observed and synthetic waveforms of the Balochistan earthquake

473 **Figure S2.** Fitting between observed and synthetic waveforms of the Gorkha earthquake

474 **Table S1.** Velocity structure in the source region of the 2013 Balochistan earthquake

475 **Table S2.** Velocity structure in the source region of the 2015 Gorkha earthquake



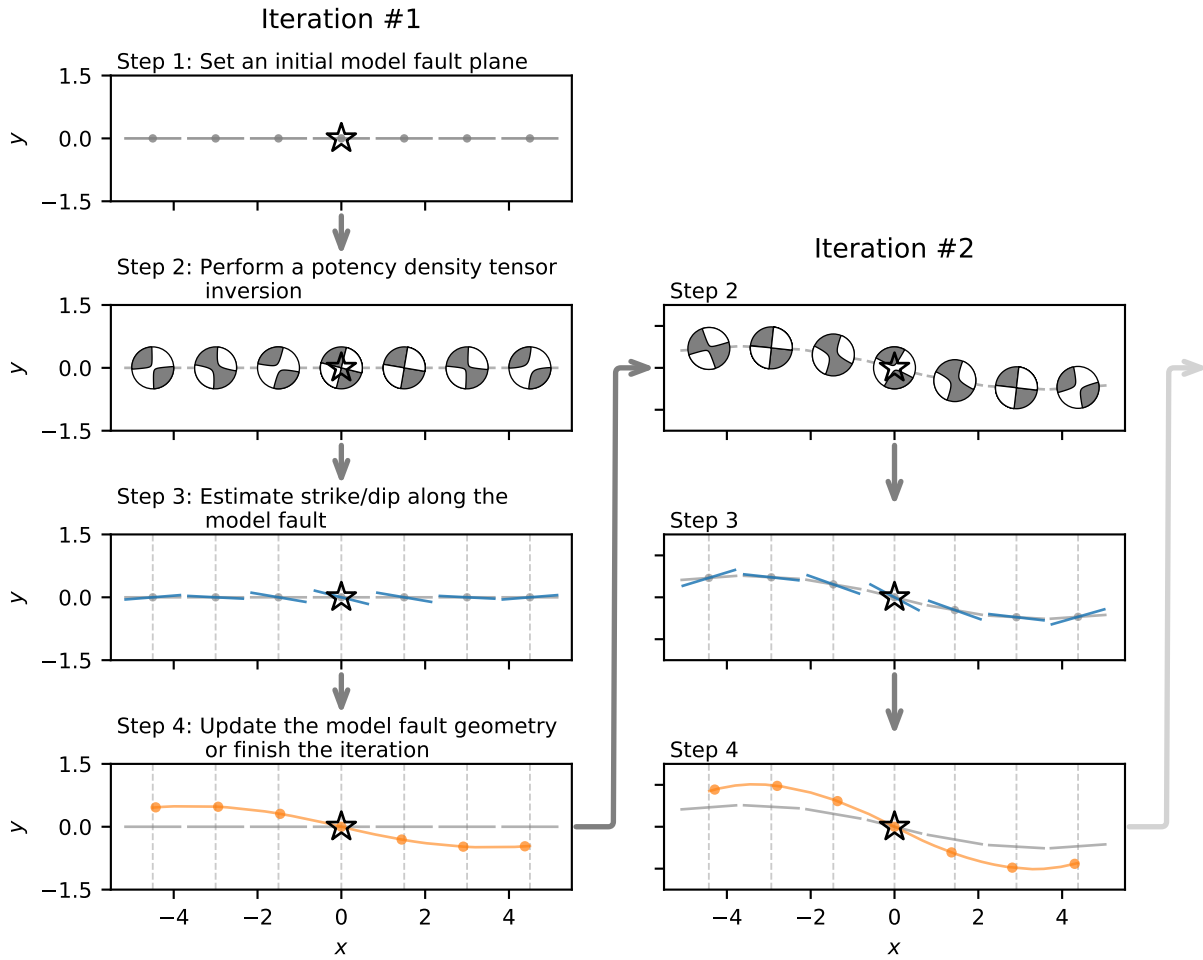


**Figure 1.** Schematic illustration of the workflow of the iterative inversion process to construct fault geometry. The  $x$  axis is the distance from the hypocentre along the strike (or dip) direction of the initial flat model-fault plane. The  $y$  axis is the displacement of the updated model fault plane perpendicular to the  $x$  axis. The star denotes the location of the hypocentre. Grey bars with grey circles at their midpoints represent subfaults of the model fault plane used in the finite-fault inversion analysis. The beach ball at each subfault in step 2 represents a focal mechanism obtained by the finite-fault inversion of Shimizu et al. (2020). In step 3 we select one of the nodal planes (blue line) of the double-couple components to represent the fault geometry from the focal mechanism obtained in step 2. The orange line in the step 4 represents the updated fault geometry determined by spline interpolation with quadratic functions. The orange line of this iteration is used as the model fault geometry in the next iteration.

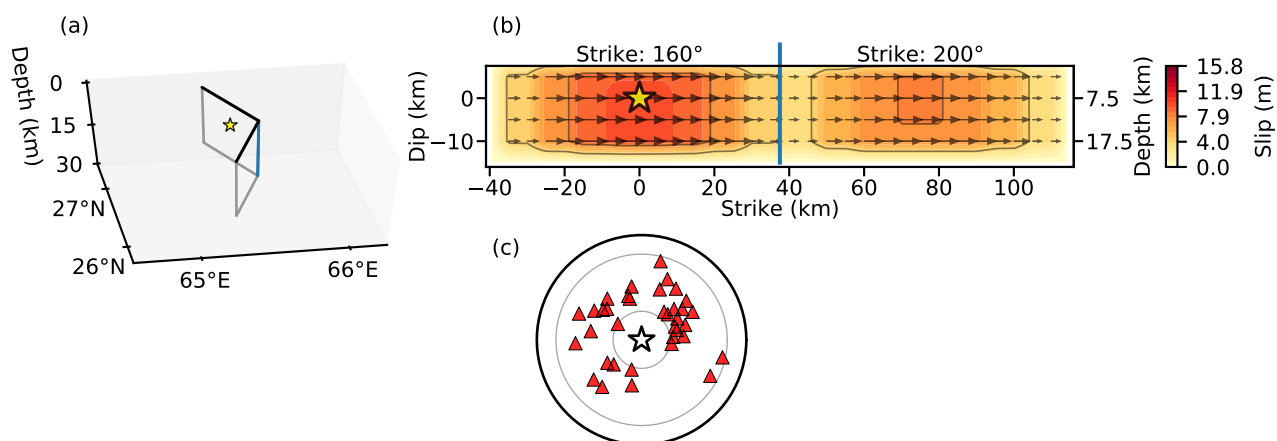


**Figure 2.** Input source model for case 1. (a) Fault geometry. The input fault plane consists of two vertical rectangles with different strikes that meet the surface along the black lines and intersect on the blue line. The yellow star denotes the hypocentre. (b) Slip distribution on the input fault plane; contour interval is 4 m. The arrows are slip vectors, and the star denotes the hypocentre. (c) Station distribution (red triangles) around the epicentre (star) in an azimuthal equidistant projection. The grey circles indicate the 30° and 90° teleseismic distances.

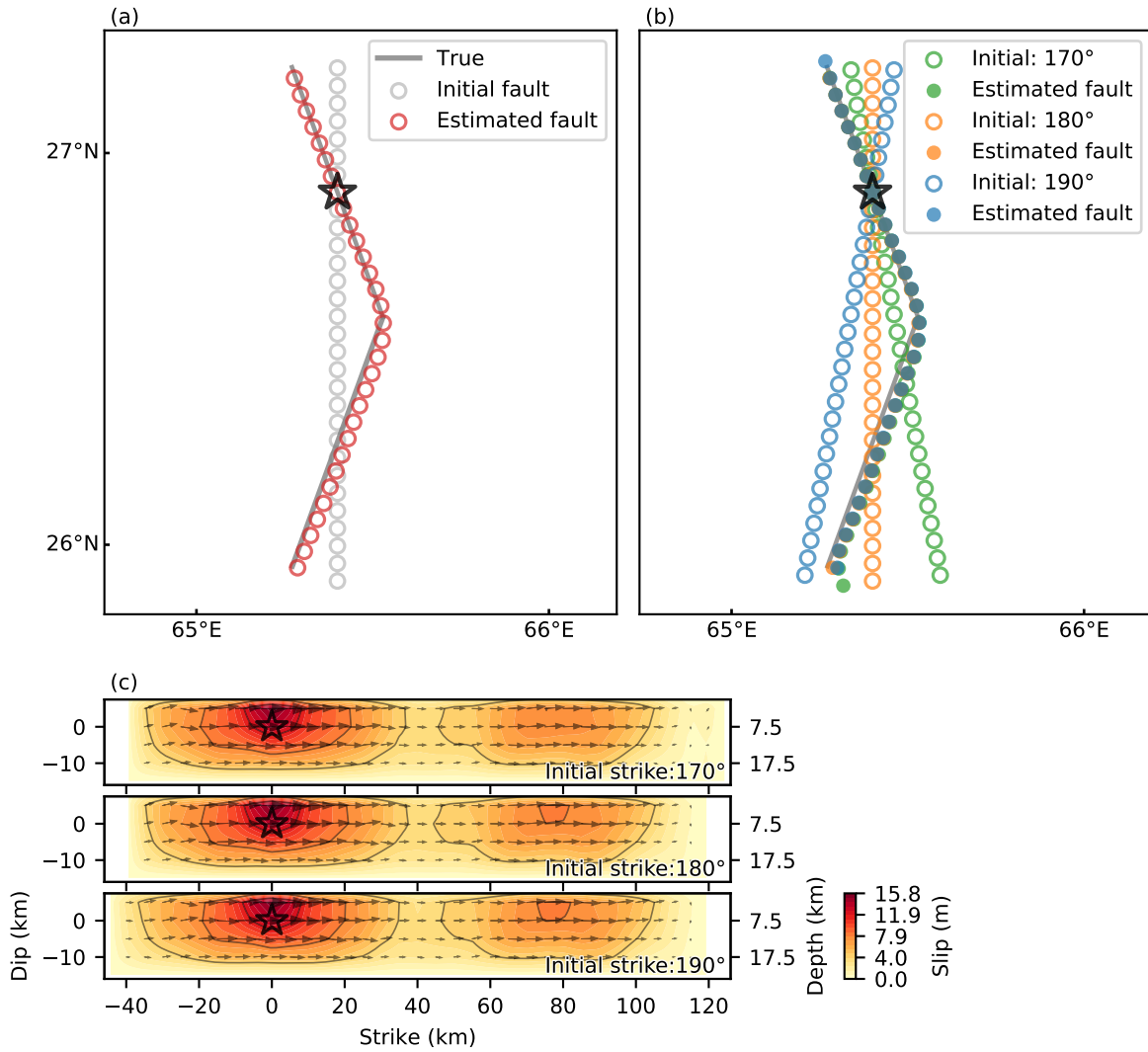


**Figure 3.** Results of synthetic test case 1. (a) True, initial, and estimated fault traces. The grey line represents the trace of the true fault plane. Grey and red circles represent the central points of subfaults of the initial and estimated model fault planes, respectively. The star denotes the epicentre. (b) Sensitivity of results to the strike of the initial model fault plane. All three initial fault planes (open circles) yield estimated fault traces (filled circles) that are nearly indistinguishable at the scale of this plot. (c) Estimated slip distribution on the model fault plane; contour interval is 4 m. The arrows represent slip vectors.

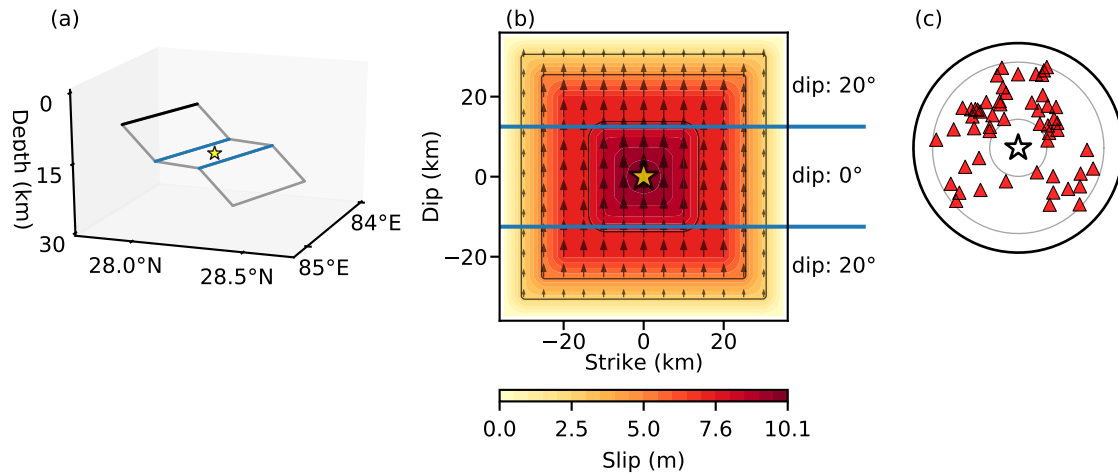


**Figure 4.** Input source model for case 2. (a) Fault geometry. The input fault plane consists of three rectangles with a ramp-flat-ramp structure. Black and blue lines are top of model fault and intersections of sub-planes, respectively. The yellow star denotes the hypocentre. (b) Slip distribution on the input fault plane; contour interval is 2.5 m. The arrows represent slip vectors. (c) Station distribution (red triangles) around the epicentre (star) in an azimuthal equidistant projection. The grey circles indicate the 30° and 90° teleseismic distances.

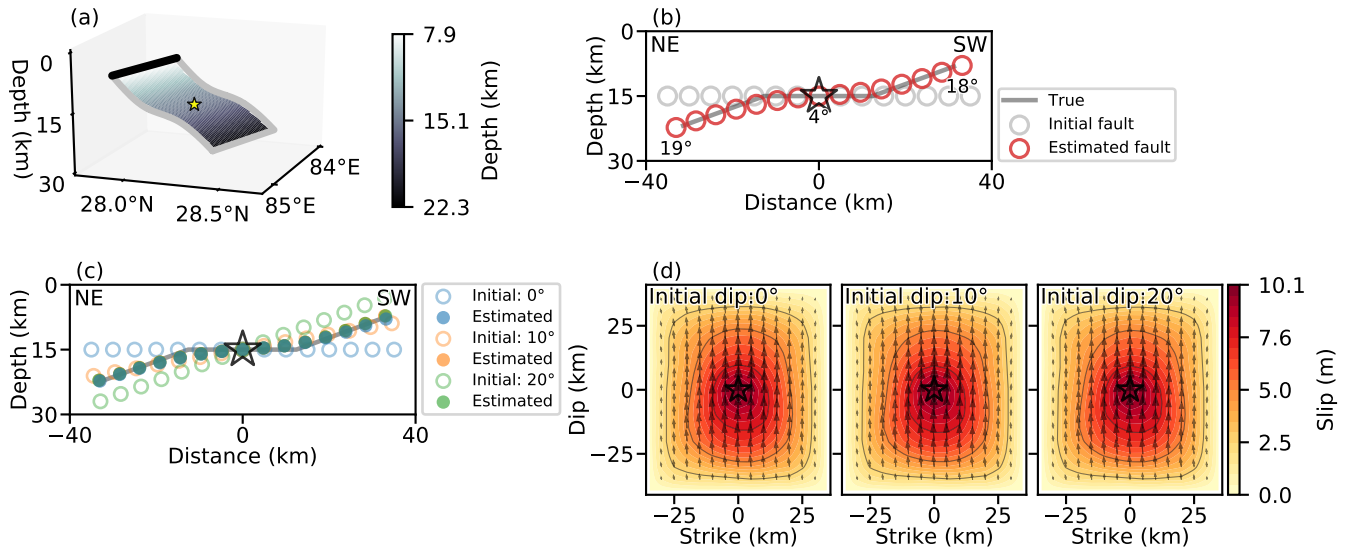


**Figure 5.** Results of synthetic test case 2. (a) Estimated fault geometry. The star denotes the hypocentre. (b) Cross sections of the true, initial, and estimated fault planes. (c) Sensitivity of results to the dip of the initial fault plane. All three initial fault planes (open circles) yield estimated fault traces (filled circles) that are indistinguishable at the scale of this plot. (d) Estimated slip distribution on the model fault plane; contour interval is 2.5 m. The arrows represent slip vectors.

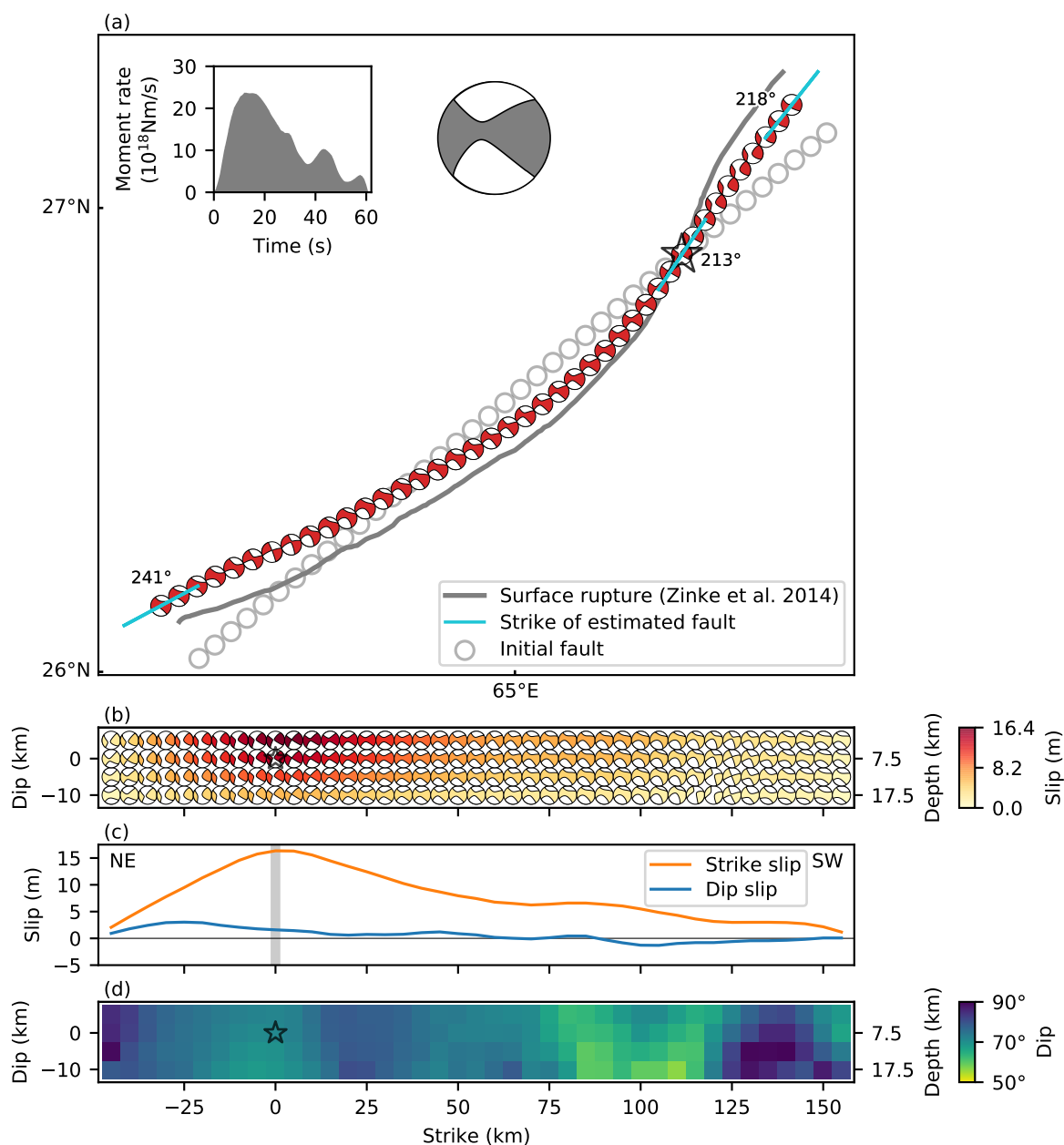


**Figure 6.** Source model of the 2013 Balochistan earthquake estimated by the proposed method. (a) The initial fault geometry is shown by grey circles at the centre of subfaults. The small beachball symbols show the focal mechanisms of the subfaults on the estimated fault trace, obtained by integrating the potency density tensors, shown in (b), with respect to the dip direction. Blue bars and numbers indicate the strike of the subfaults at the hypocentre and both ends of the estimated fault. The large beachball symbol shows the total potency tensor of the earthquake, obtained by integrating the potency density tensors shown in (b), over the fault plane. The grey line represents the surface rupture trace observed by Zinke et al. (2014). The inset shows the estimated moment rate function of the earthquake. The star denotes the epicentre. (b) Distribution of potency density tensors on the estimated fault plane. Beachball symbols indicate the focal mechanism at each subfault and their colour indicates the slip amount. (c) Profiles along the model fault trace of the strike-slip and dip-slip components, estimated from the potency density tensors at the top of the fault plane. The strike-slip component is positive for left-lateral faulting, and the dip-slip component is positive for reverse faulting. The grey vertical bar represents the location of the epicentre. (d) Distribution of dip (colour) on the estimated fault plane.

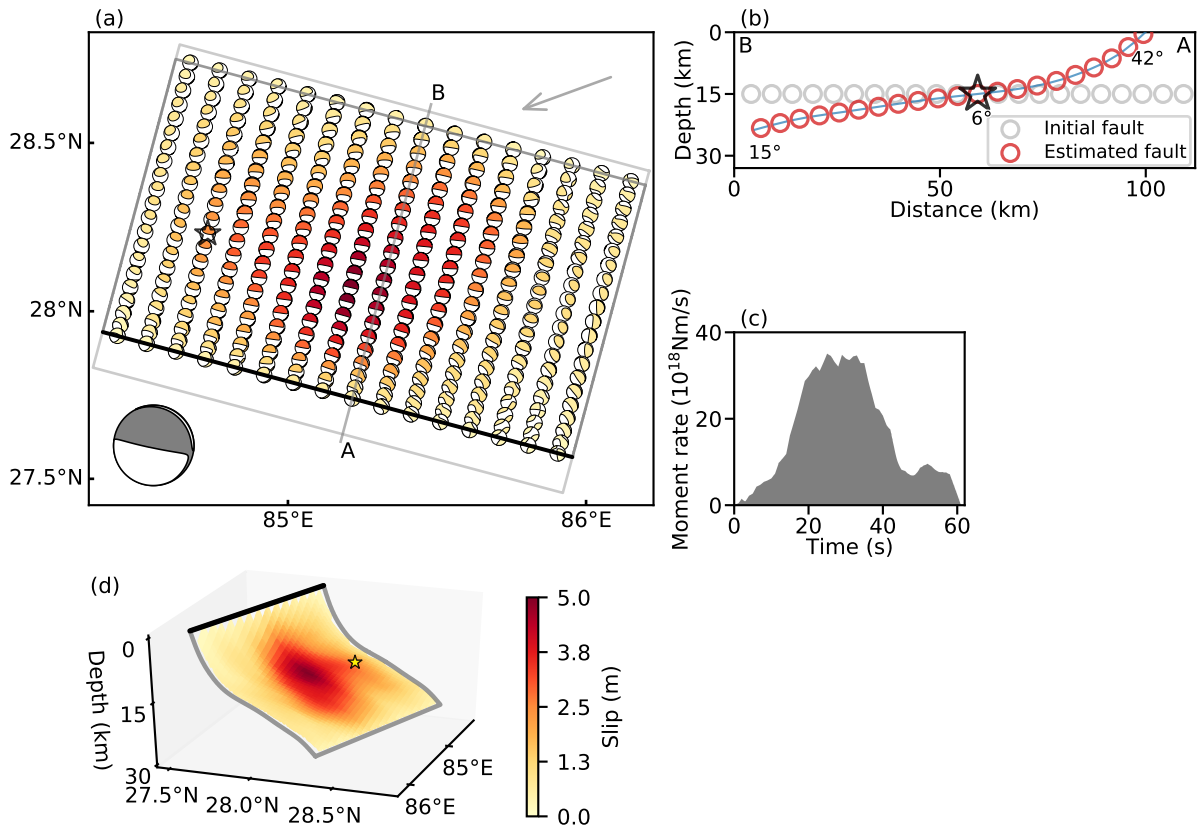


**Figure 7.** Source model of the 2015 Gorkha earthquake estimated by the proposed method. (a) Distribution of potency density tensors on the estimated fault plane. The light grey line outlines the initial fault plane. Small beachball symbols indicate the focal mechanism for each subfault and their colour indicates the slip amount according to the colour scale in (d). The large beachball symbol shows the total potency tensor of the earthquake, obtained by integrating the potency density tensors over the fault plane. Arrow indicates azimuth of 3D view of (d). (b) Cross section of the model-fault plane along line A–B in (a). Grey and red circles represent the central points of subfaults of the initial and estimated model fault planes, respectively. Blue bar indicates the dip of each subfault. Denoted numbers are dip angles at the hypocentre and both ends of the estimated fault. (c) Estimated moment rate function of the earthquake. (d) Estimated fault geometry and slip amount (colour) viewed from the north-east indicated by the arrow in (a).

Supporting Information for

## **Construction of fault geometry by finite-fault inversion of teleseismic data**

Kousuke Shimizu,<sup>1</sup> Yuji Yagi,<sup>2</sup> Ryo Okuwaki,<sup>2,3,4</sup> and Yukitoshi Fukahata<sup>5</sup>

<sup>1</sup>*Graduate School of Life and Environmental Sciences, University of Tsukuba, Tsukuba, Ibaraki 305-8572, Japan.*

*E-mail: seismo55smz@gmail.com*

<sup>2</sup>*Faculty of Life and Environmental Sciences, University of Tsukuba, Tsukuba, Ibaraki 305-8572, Japan.*

<sup>3</sup>*Mountain Science Center, University of Tsukuba, Tsukuba, Ibaraki 305-8572, Japan.*

<sup>4</sup>*COMET, School of Earth and Environment, University of Leeds, Leeds LS2 9JT, UK.*

<sup>5</sup>*Disaster Prevention Research Institute, Kyoto University, Uji, Kyoto 611-0011, Japan.*

### **CONTENTS**

**Figure S1** Fitting between observed and synthetic waveforms of the Balochistan earthquake

**Figure S2** Fitting between observed and synthetic waveforms of the Gorkha earthquake

**Table S1** Velocity structure in the source region of the 2013 Balochistan earthquake

**Table S2** Velocity structure in the source region of the 2015 Gorkha earthquake



2013 Balochistan earthquake

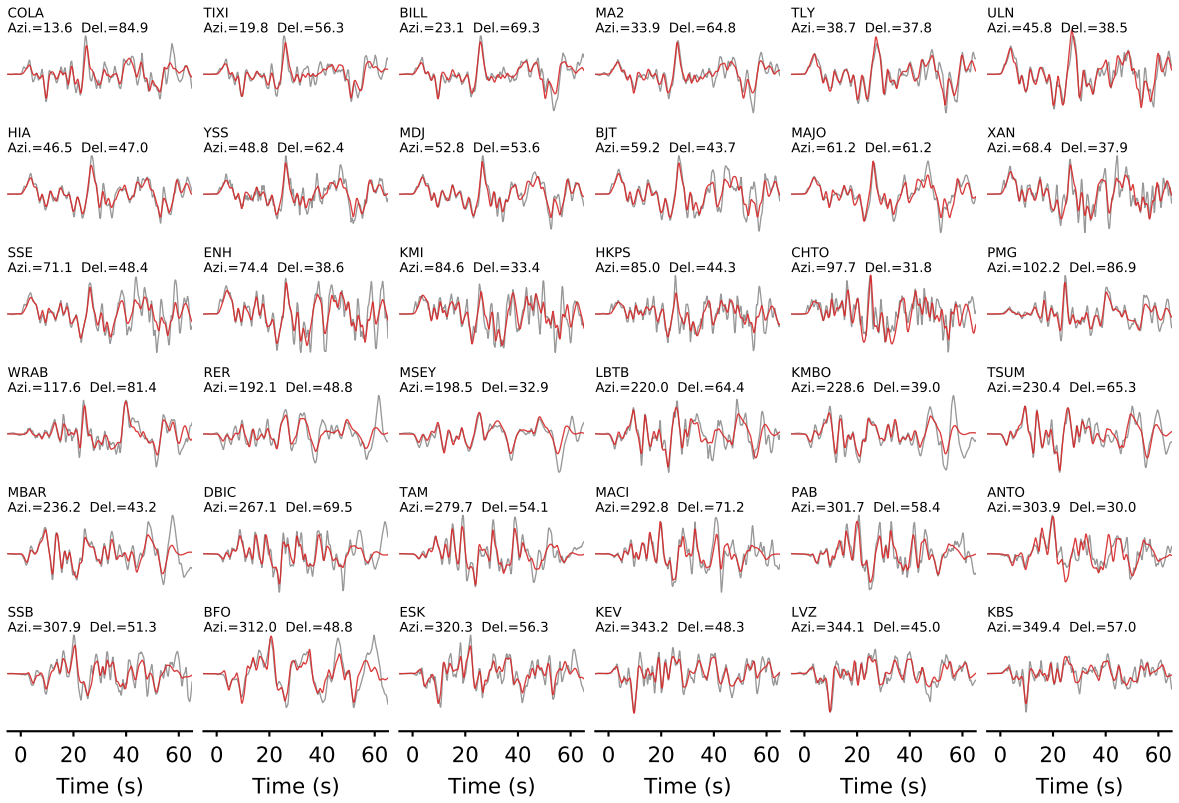


**Figure S1.** Waveform fitting at all stations between observed (gray line) and synthetic waveforms (red line) in the analysis of the Balochistan earthquake by using the constrained fault model. The waveforms are plotted with a sampling interval of 0.05 s. Station code, azimuth, and epicentral distance are shown above the traces.

## 2015 Gorkha earthquake

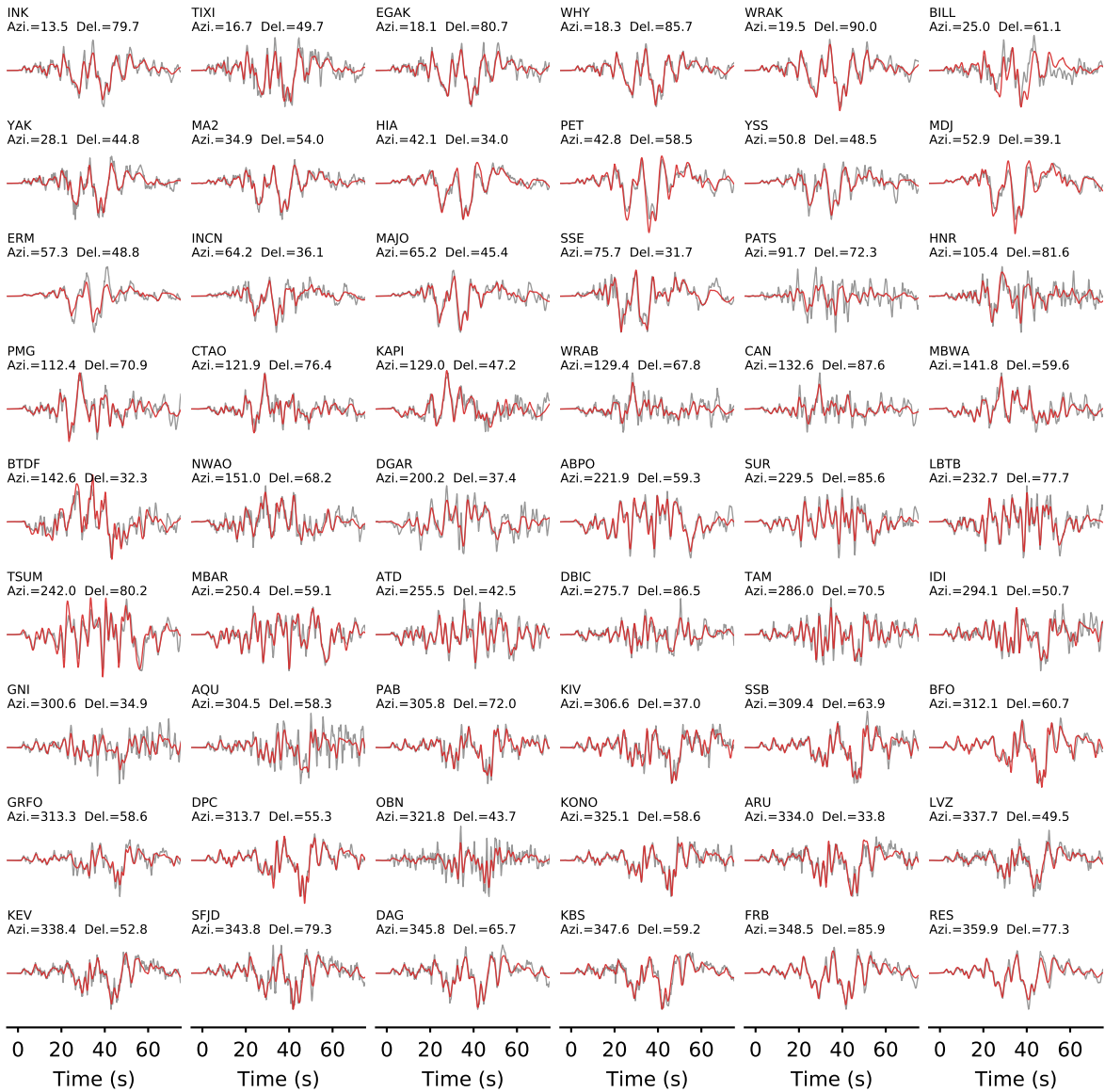


**Figure S2.** Waveform fitting at all stations between observed (gray line) and synthetic waveforms (red line) in the analysis of the Gorkha earthquake. The waveforms are plotted with a sampling interval of 0.05 s. Station code, azimuth, and epicentral distance are shown above the traces.

**Table S1.** Near-source velocity model from Avouac et al. (2014) used for calculating Green's functions.

$V_P$ (km/s)	$V_S$ (km/s)	Density ( $10^3\text{kg/m}^3$ )	Thickness (km)
5.44	3.00	2.50	4.00
6.25	3.45	2.60	12.00
6.53	3.60	2.70	14.00
6.80	3.90	2.90	12.00
7.50	4.30	2.90	3.00
8.11	4.49	3.30	0.00

**Table S2.** Near-source velocity model from CRUST1.0 (Laske et al. 2013) used for calculating Green's functions.

$V_P$ (km/s)	$V_S$ (km/s)	Density ( $10^3\text{kg/m}^3$ )	Thickness (km)
6.00	3.52	2.72	27.25
6.30	3.68	2.79	13.08
6.60	3.82	2.85	14.17
8.44	4.68	3.45	0.00

## REFERENCES

- Avouac, J. P., Ayoub, F., Wei, S., Ampuero, J. P., Meng, L., Leprince, S., Jolivet, R., Duputel, Z., & Helmberger, D., 2014. The 2013, Mw 7.7 Balochistan earthquake, energetic strike-slip reactivation of a thrust fault, *Earth and Planetary Science Letters*, **391**, 128–134.
- Laske, G., Masters, G., Ma, Z., & Pasyanos, M., 2013. Update on CRUST1.0—A 1-degree global model of Earth's crust, *EGU General Assembly 2013*, **15**, 2658.